PNAS RESEARCH ARTICLE | ENGINEERING

A self-resetting soft ring for autonomous, continuous leaping in unstructured environments

Fangjie Qi[a], Caizhi Zhou[a], Haitao Qing[a], Haoze Sun[a], Yaoye Hong[a], and Jie Yin[a,1]

Affiliations are included on p. 11.

Edited by Michael D. Bartlett, Virginia Tech, Blacksburg, VA; received March 5, 2026; accepted July 24, 2026 by Editorial Board Member Joanna Aizenberg

Continuous leaping is an effective locomotion strategy for traversing cluttered and unstructured environments. However, achieving autonomous continuous leaping in soft machines remains challenging because it requires recyclable energy storage and release, reliable self-resetting for relaunch, aerial stability, and adaptability across diverse terrains. Here, we report a self-resetting soft ring jumper capable of autonomous, continuous, and stable horizontal leaping under constant infrared illumination. The jumper consists of a photothermally responsive liquid crystal elastomer ring integrated with a rigid V-shaped tail. Under illumination, the soft ring self-twists to store elastic energy while simultaneously inducing out-of-plane bending of the tail through geometric constraints imposed by the rigid tail. Once a critical threshold is reached, snapping of the rotating rigid tail against the ground launches the ring into the air. During flight, the ring autonomously untwists to recover its original shape and self-resets, enabling repeated cycles of energy storage, release, and relaunch. The snapping mechanism and full leaping dynamics are captured by combined static and dynamic Cosserat-rod models. By tuning geometric asymmetry and the center of mass, the jumper transitions among crawling, directional leaping, and vertical jumping. Optimized designs achieve vertical jumps exceeding 80 body heights and directional leaps over 3 body lengths. Beyond controlled motion on flat surfaces, the jumper demonstrates resilient multimodal locomotion across slopes, parallel hurdles, water–land interfaces, and diverse natural terrains including grass, sand, rocks, mulch, and water surfaces. This work can find potential applications in environmental navigation, swarm robotics, and unstructured terrain navigation.

continuous soft leaper | self-resetting | snapping | asymmetric ring geometry | multimodal locomotion

Significance

Autonomous repetitive jumping in soft material systems remains challenging because most designs require external resetting, complex control, or spatiotemporal stimulation. Here, we show that a simple self-resetting V-shaped ring geometry can achieve continuous, terrain-adaptive leaping under constant illumination. By coupling photothermal twisting of the ring with tail bending imposed by asymmetric geometric constraints, the system autonomously stores, releases, and recycles elastic energy through snap-through instability for repeated launching, landing, recovery, and relaunch without external control. The geometry-enabled design further provides collision resilience, directional adaptability, and robust locomotion across diverse natural terrains and land–water interfaces. More broadly, this work establishes a general framework for self-resetting energy recycling and physical intelligence in soft active materials for autonomous operation in complex environments.

Jumping is a powerful locomotion strategy in nature, enabling organisms to traverse long distances rapidly and navigate complex terrains. The underlying principle is universal: elastic energy is stored and suddenly released to generate a power-amplified burst of motion. Energy can be stored through bending, stretching, or twisting (1–4), and released through distinct mechanisms such as snapping instabilities (1, 2, 4–9), latching (2, 3, 10), fracturing (11), and explosion (12, 13). To enable repetitive leaping, animals rely on active muscular or latch-based reloading for resetting (14), while plants achieve passive resetting and limited repeatability via environmentally driven material responses to cyclic humidity changes (15, 16).

Inspired by these strategies, researchers have developed soft jumping systems using stimuli-responsive materials such as liquid crystal elastomers (LCEs) (17–21), hydrogels (11), electroactive polymers (22), and magneto-elastomers (7, 23). Yet a central challenge persists achieving autonomous, continuous, and adaptive leaping without latches, active stimulus modulation, or human intervention. Analogous to the origami "paper frog" (*SI Appendix*, Fig. S1 and Movie S1), which jumps once before requiring manual resetting, most soft jumpers are effectively single-shot devices. It requires manual resetting or dynamic modulation of external stimuli to operate repetitively in either tethered or untethered modes (3, 7, 11, 18, 20, 22, 24–26). Recent advances demonstrate novel strategies, such as evaporating elastomeric disks that self-snap to bounce a few times (27), combustion-powered jumpers (13) that leap forcefully but only for limited cycles, or self-shuttering for light-responsive repeated upright jumping (28). However, none achieve sustained, adaptive, and autonomous leaping in unstructured environments under a constant field.

Several obstacles underpin this challenge. First, energy resetting under constant stimulation is inherently difficult: most engineered jumpers require time-varying stimuli or manual flipping between bistable states to recover shape (3, 7, 11, 18, 20, 22, 24, 25), complicating both actuation and control. Second, aerial posture regulation is critical: body orientation during flight dictates landing state, and without stable recovery, sustained and directional leaping is impossible. Third, sustained leaping in unstructured environments

Author contributions: F.Q. and J.Y. designed research; F.Q. and C.Z. performed research; C.Z. and Y.H. contributed new reagents/analytic tools; F.Q., C.Z., H.Q., H.S., and Y.H. analyzed data; and F.Q., C.Z., and J.Y. wrote the paper.

The authors declare no competing interest.

This article is a PNAS Direct Submission. M.D.B. is a guest editor invited by the Editorial Board.

[1]To whom correspondence may be addressed. Email: jyin8@ncsu.edu.

This article contains supporting information online at https://www.pnas.org/lookup/suppl/doi:10.1073/pnas.2607940123/-/DCSupplemental.

Published August 27, 2026.

requires self-adaptability and robustness against uneven terrains and obstacles, preventing trapping or motion arrest. Overcoming these barriers is crucial for achieving continuous, autonomous soft jumping beyond controlled settings.

Here, we leverage the asymmetric geometry of a V-shaped soft ring to achieve self-resetting directional jumping under constant external fields (Fig. 1 *A* and *B* and Movie S1). Under uniform infrared illumination, the ring self-twists to store elastic energy while bending the rigid tail inward. Snapping of the tail against the ground rapidly releases the stored energy to launch the ring, while in-flight untwisting restores its original shape for autonomous resetting and continuous relaunching (Fig. 1 *B–D*). Unlike conventional soft jumpers that rely on bistability, latching, or temporally modulated stimuli (3, 7, 11, 18, 20, 22, 24–26), the present system encodes self-resetting directly into its V-shaped ring topology, enabling sustained cyclic energy storage and release under constant illumination. By tuning geometric asymmetry and mass distribution, we realize stable directional leaping. Beyond sustained leaping, the soft ring demonstrates robust, self-adaptive multimodal locomotion across slopes, obstacles, natural terrains, and land–water interfaces, providing a generalizable framework for autonomous, sustained soft machines powered by uniform energy fields.

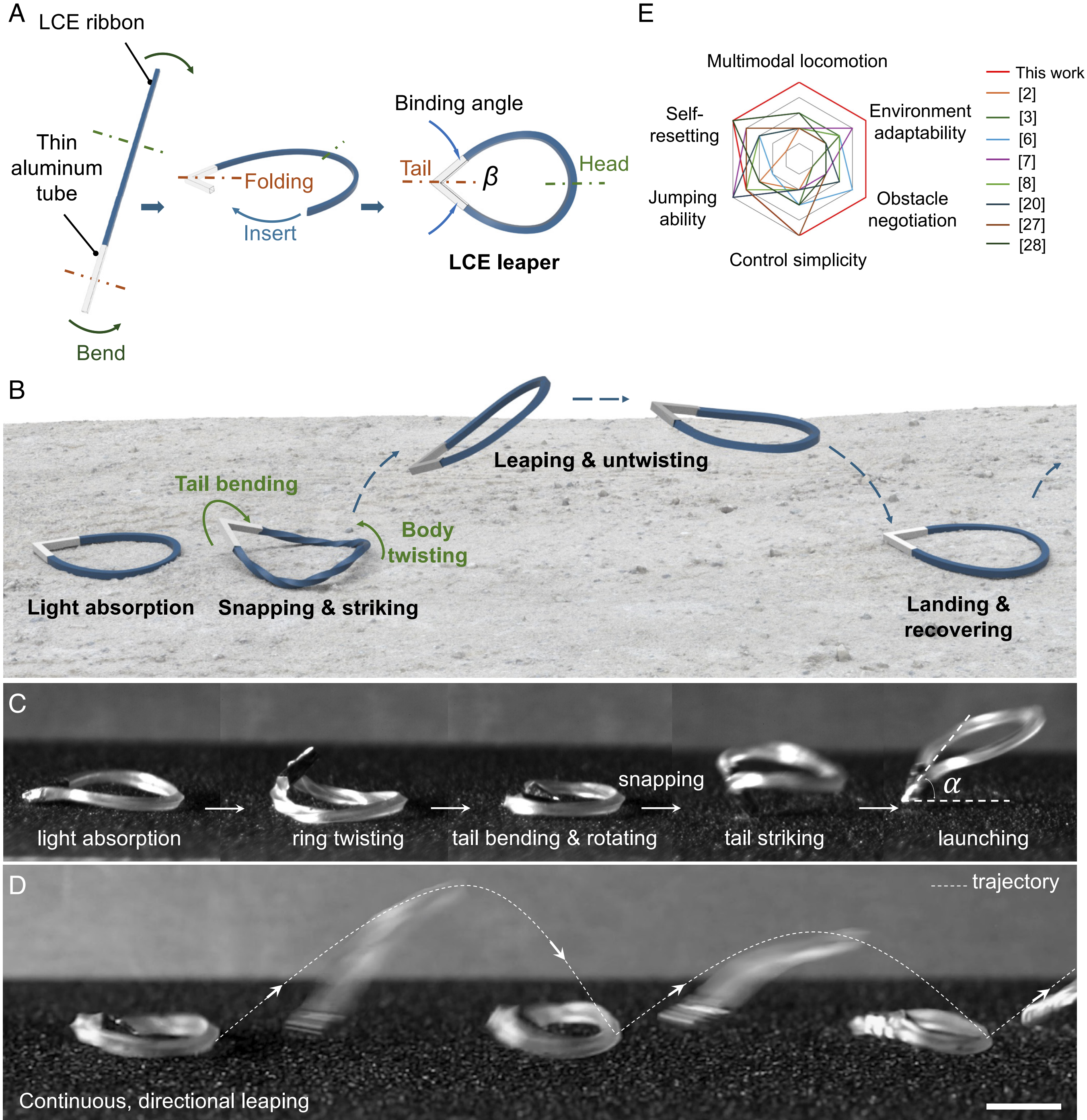

Fig. 1. Self-resetting soft ring for continuous and autonomous leaping. (*A*) Schematics of fabricating the V-shaped jumping ring. (*B*) Schematics of self-resetting and continuous leaping under constant infrared illumination. (*C*) High-speed image sequence of the launch process. (*D*) Continuous, directional leaping tracked under constant illumination. Dashed lines mark head trajectories. (Scale bar, 5 mm.) (*E*) Radar chart on the multidimensional comparison between existing soft jumpers and this work.

Results

Continuous Leaping of the Soft Ring. The V-shaped soft ring is fabricated by bending and joining the ends of a soft LCE rod with a short aluminum tube, thereby creating a sharp binding angle β that breaks circular symmetry (Fig. 1*A* and *SI Appendix*, Fig. S2). The structure integrates a soft, deformable LCE segment as the main body (body length 20 mm and body height 1 mm) with a rigid aluminum sheet-reinforced segment as a V-shaped tail (*SI Appendix*, Fig. S3 and *Note S1* and *Methods*). The geometric constraint imposed by the tail's rigidity and sharp angle raise the energy barrier for release, allowing higher elastic energy accumulation and enhancing the striking force against the ground (Fig. 1*B* and Movie S1).

Under uniform infrared (IR) illumination maintained at constant intensity throughout all jumping cycles, without external switching or temporal modulation (*SI Appendix*, Fig. S4), the ring body undergoes photothermal heating-induced anisotropic shrinking, flipping outside-in due to temperature gradients (29–31) and progressively storing strain energy through torsional twisting (Fig. 1*C*) (*SI Appendix*, Fig. S5 and *Note S2* and *Methods*). Meanwhile, the rigid tail, resisting twist, simultaneously bends out of plane and rotates upward toward the ring's center (Fig. 1*C*). When beyond a threshold, it snaps inward within ~30 ms, rapidly releasing stored energy to strike the surface and propel the ring into the air with a launching angle α ~47° (β = 100°, light intensity w = 0.6 W cm^{-2}, Fig. 1*C*).

Crucially, once in air, the ring relaxes back to its original shape, resetting the geometry automatically before landing (Fig. 1 *C* and *D*). It achieves a horizontal jumping distance of ~34 mm, i.e., ~1.7 body lengths (BLs). Under continuous illumination, the cycle repeats: coupled twisting and bending store energy on ground, followed by in-air untwisting that restores the initial configuration (Fig. 1*D*). This closed, limit-cycle process enables fully autonomous and repetitive leaping (over 500 jumps) without latches, external modulation, or manual resetting (*SI Appendix*, Fig. S6 and Movie S2). Compared with existing soft jumpers, the simple ring design uniquely combines exceptional self-resetting capability with minimal control, high jumping performance, collision resilience, adaptability to diverse unstructured terrains, and multimodal locomotion across both land and water surfaces (Fig. 1*E* and *SI Appendix*, *Note S3*), as discussed later.

Locomotion Phase Diagram. The interplay between geometry and energy input governs the ring's locomotion modes. By varying the binding angle β, which sets the geometric asymmetric and energy barrier, and the light intensity w, which controls actuation power, we map a phase diagram spanning vertical jumping, horizontal leaping, and crawling (Fig. 2 *A–G*).

At low-to-moderate light intensity (0.4 to 0.6 W cm^{-2}), increasing β from 30° to 130° drives a clear transition (Fig. 2*A* and Movie S3 and *SI Appendix*, *Note S4*): sharp tails enable vertical jumps (30° ≤ β ≤ 80°, Fig. 2 *C* and *H*), intermediate β produce leaping (80° < β < 110°, Fig. 2 *D–F* and *I–K*), and near-circular rings crawl (110° < β ≤ 130°, Fig. 2*G*). For small β, V-shaped tails raise the energy barrier, allowing greater torsional and bending energy storage before release (Fig. 2*C*). At sharper angles of 30° to 80°, the rings execute powerful vertical jumps. At liftoff, the soft body straightens with a launch angle of ~90°, reaching heights above 80 body heights (BHs) at β = 60°, often with in-air flips (Fig. 2 *C* and *H* and Movie S3). This performance is enabled by a self-locking effect in which the rotating tail briefly presses against the head before ground contact, delaying release for more energy accumulation that amplifies the strike, while untwisting of the ring resets the body mid-air for repetitive vertical jumping. Compared to moderate angles of ~150° in both head twist (ϕ_H) and tail rotation (ϕ_T, Fig. 2*L*), the soft ring body bends severely into a full circle to facilitate the self-locking (Fig. 2*C*). At large β (110° to 130°), the rings approach circularity and behave as slow crawlers without exhibiting snapping (Fig. 2*G*). Between these extremes lies a narrow leaping window (80° to 110°), where stored energy propels the ring forward rather than straight upward. At β ≈ 95°, the ring launches at ~50° with a straight body, producing ~72 mm leaps (~3.6 BLs) but also a 180° backflip that reverses relaunching orientation upon landing (Fig. 2 *D* and *I*). The backflip is due to the highly stored torsion energy, as observed in the excessive head twisting angle ϕ_T~550° before striking the ground (Fig. 2*M*).

Light intensity further modulates leap stability at a given β (Fig. 2*A*). For β ≈ 95°, reducing w from 0.49 to 0.41 W cm^{-2} lowers stored energy, suppressing flips, and enables stabilized forward leaps of ~2 BLs at a consistent ~53° launch angle (Fig. 2*E*). During liftoff, the head bends forward to maintain heading in flight, with the tail landing first (Fig. 2*J*). At higher intensities (~0.58 W cm^{-2}), thermal softening decreases the launch angle (~20°) and shortens leap distances (~1.1 BL) (Fig. 2 *F* and *K*), as evidenced by the dramatically reduced head twisting angles (Fig. 2 *N* and *O*). Such leap stability at a given β can also be modulated by changing the tail length for tuning energy storage (*SI Appendix*, Fig. S7). At very high intensities (w > 0.65 W cm^{-2}), shrinkage-induced interlocking suppresses forward motion in rings with intermediate β (80° to 100°), reducing them to low-amplitude vertical hopping, while rings with small β (30° to 70°) overheat and become immobile (Fig. 2*A*).

Thus, an optimal intermediate intensity (w ≈ 0.49 W cm^{-2}) maximizes elastic energy storage across a broad range of β (55° to 110°), enabling jumps of 10 to 80 BHs (10 to 80 mm). This locomotion phase diagram illustrates how geometry and energy input cooperatively govern transitions between crawling, leaping, and vertical jumping.

Modeling and Simulation of Snapping and Leaping. To gain mechanistic insight into snapping in the ring jumper, we employ both dynamic and static Cosserat-rod models (32) to capture the rapid elastic-to-kinetic energy conversion during snap-through and predict the snapping phase diagrams (*SI Appendix*, *Notes S5 and S6*). The ring body with length L is modeled as an elastically deformable rod, whereas the V-shaped tail with length L_1 and binding angle β is treated as a rigid body fixed to the ground. Owing to the symmetry of the twisted configuration, the full ring is reduced to a half-rod model (*SI Appendix*, Fig. S8). One end of the rod is rigidly attached to the tail, while the other end is constrained by a planar joint on the symmetric plane. Actuation is represented by imposing a prescribed twist angle θ_z at the planar joint (*SI Appendix*, Fig. S8). The governing equations including kinematics, compatibility, force and momentum balance, and constitutive relations are provided in the *SI Appendix*, *Notes S5 and S6*. Boundary conditions are imposed at both the tail-attached end and the symmetry-plane end:

$$ {}^{A}_{1}\boldsymbol{T} = \boldsymbol{R}_x\left(-\pi - \frac{\beta}{2}\right)\boldsymbol{D}_z(L_1), \quad [1]$$

$$ {}^{A}_{n+1}\boldsymbol{T} = \boldsymbol{R}_x(-\pi)\boldsymbol{R}_z(-\theta_z)\boldsymbol{D}_x(d_x)\boldsymbol{D}_y\left(d_y\right), \quad [2]$$

$$ F^{x}_{n+1} = F^{y}_{n+1} = 0, \quad [3]$$

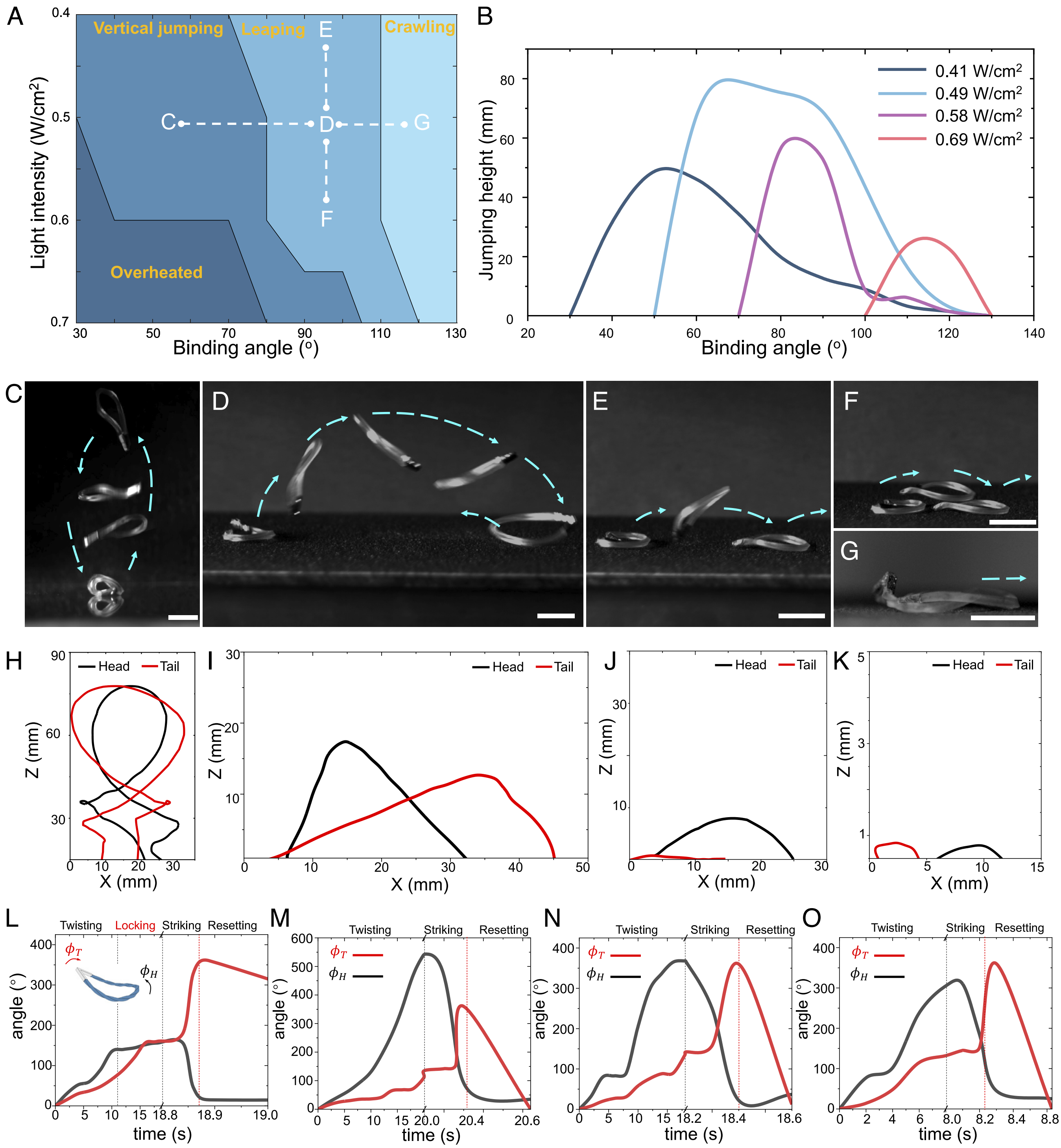

Fig. 2. Locomotion phase diagram governed by geometry and illumination. (*A*) Phase diagram showing transitions among continuous vertical jumping, horizontal leaping, and crawling as functions of binding angle β and light intensity w. (*B*) Jumping height as a function of β under varying w. (*C–G*) Corresponding optical images of jumping and crawling rings in *A*. (*H–K*) Corresponding head and tail trajectories for the motions shown in *C–F*. (*L–O*) Corresponding head (ϕ_H) and tail (ϕ_T) rotating angle changes with actuation time for the motions shown in *C–F*. (Scale bar, 10 mm.)

$$\boldsymbol{v}(0) = 0, \ \ \boldsymbol{\Omega}(0) = 0, \qquad [4]$$

where $\boldsymbol{T}$ is the transformation matrix of the material frame expressed in the global frame $\{A\}$. $\boldsymbol{R}_{\mathrm{i}}$ and $\boldsymbol{D}_{\mathrm{i}}$ denote homogeneous rotation and translation transformations, respectively. d_i is unknown sliding displacements of the distal end on the symmetry plane. F^i_{n+1} denotes the force components exerted at the rod endpoints. ν and Ω are the translational and angular velocities, respectively.

The elastic energy stored in the rod U and the kinetic energy T are computed as

$$U = \frac{1}{2}\int_0^L (\boldsymbol{\eta}-\overline{\boldsymbol{\eta}})^T \boldsymbol{K}_\eta (\boldsymbol{\eta}-\overline{\boldsymbol{\eta}}) + (\boldsymbol{\omega}-\overline{\boldsymbol{\omega}})^T \boldsymbol{K}_\omega (\boldsymbol{\omega}-\overline{\boldsymbol{\omega}})\, \mathrm{d}s, \qquad [5]$$

$$T = \frac{1}{2}\int_0^L \rho A\, \boldsymbol{v}^T \boldsymbol{v} + \boldsymbol{\Omega}^T \rho \boldsymbol{J} \boldsymbol{\Omega}\, \mathrm{d}s, \qquad [6]$$

where the vectors η and ω are the translational and angular strains, respectively. The material is modeled as linearly elastic with internal damping, where $\boldsymbol{K}_\eta$ and $\boldsymbol{K}_\omega$ are the stretching/shearing and bending/twisting stiffness matrices. The natural strains are prescribed as $\overline{\boldsymbol{\eta}} = [0, 0, 1]^{\mathrm{T}}$ and $\overline{\boldsymbol{\omega}} = 0$. ρ, A, and $\boldsymbol{J}$ are the material density, cross-sectional area, and cross-sectional second-moment matrix per unit length, respectively. The governing equations are solved using an implicit time-integration scheme (32), which improves numerical stability during snap-through.

The dynamic model captures the coupled twisting and bending deformation (Fig. 3*A*), as well as the rapid elastic-to-kinetic energy conversion (Fig. 3*B*) during snap-through observed experimentally (Movie S4 and *SI Appendix, Note S6*). Starting from the initial configuration 1), increasing θ_z leads to progressive elastic energy storage accompanied by bending. The ring evolves into twisted and bended configuration 2) and eventually reaches the unstable state 3), corresponding to the maximum elastic energy. Once the angular constraint is released near state 3), the stored elastic energy is rapidly converted into kinetic energy, producing a sharp kinetic-energy peak and driving rapid snap-through toward state 4) (Fig. 3*B*).

To determine the onset of snapping and construct the snapping phase diagram, we further derive the static form of the model by removing the time-dependent terms from the governing equations while keeping the same geometric constraints and boundary conditions (*SI Appendix, Note S5*). For each prescribed θ_z, the resulting nonlinear boundary-value problem is solved by a shooting method. The unknown vector contains the initial internal force and moment together with the two sliding coordinates of the distal end, $\boldsymbol{X} = (\boldsymbol{F}_1; \boldsymbol{M}_1; d_x; d_y)$. The terminal position error, orientation error, and symmetry-force constraints form an eight-dimensional residual $\boldsymbol{G}(\boldsymbol{X}) = \boldsymbol{0}$. The snapping point is identified from the loss of regularity of the residual Jacobian,

$$\boldsymbol{J} = \frac{\partial \boldsymbol{G}}{\partial \boldsymbol{X}}. \qquad [7]$$

As θ_z increases, we monitor the smallest singular value $\sigma_{\min}(\boldsymbol{J})$ and the condition number $\kappa(\boldsymbol{J})$. A sharp decrease in $\sigma_{\min}(\boldsymbol{J})$, together with a rapid increase in $\kappa(\boldsymbol{J})$, is used as a numerical indicator that the equilibrium branch is approaching a snap-through point (*SI Appendix*, Fig. S9). Repeating this analysis for different binding angles β and ring length L generates phase diagrams of the snapping twist angle θ_{snap} (Fig. 3*C*) and the elastic energy stored (Fig. 3*D*) at snapping.

The snapping phase diagrams reveal that decreasing β or L increases the snapping angle θ_{snap} and simultaneously increases the elastic energy stored before snapping. Thus, smaller binding angles or shorter rings require larger imposed twists to reach instability and allow greater elastic energy accumulation prior to snap-through, consistent with experimental observations. Conversely, as L becomes much longer and β approaches 180°, the structure approaches an end-connected circular ring without the additional geometric constraint imposed by the V-shaped tail. In this limit,

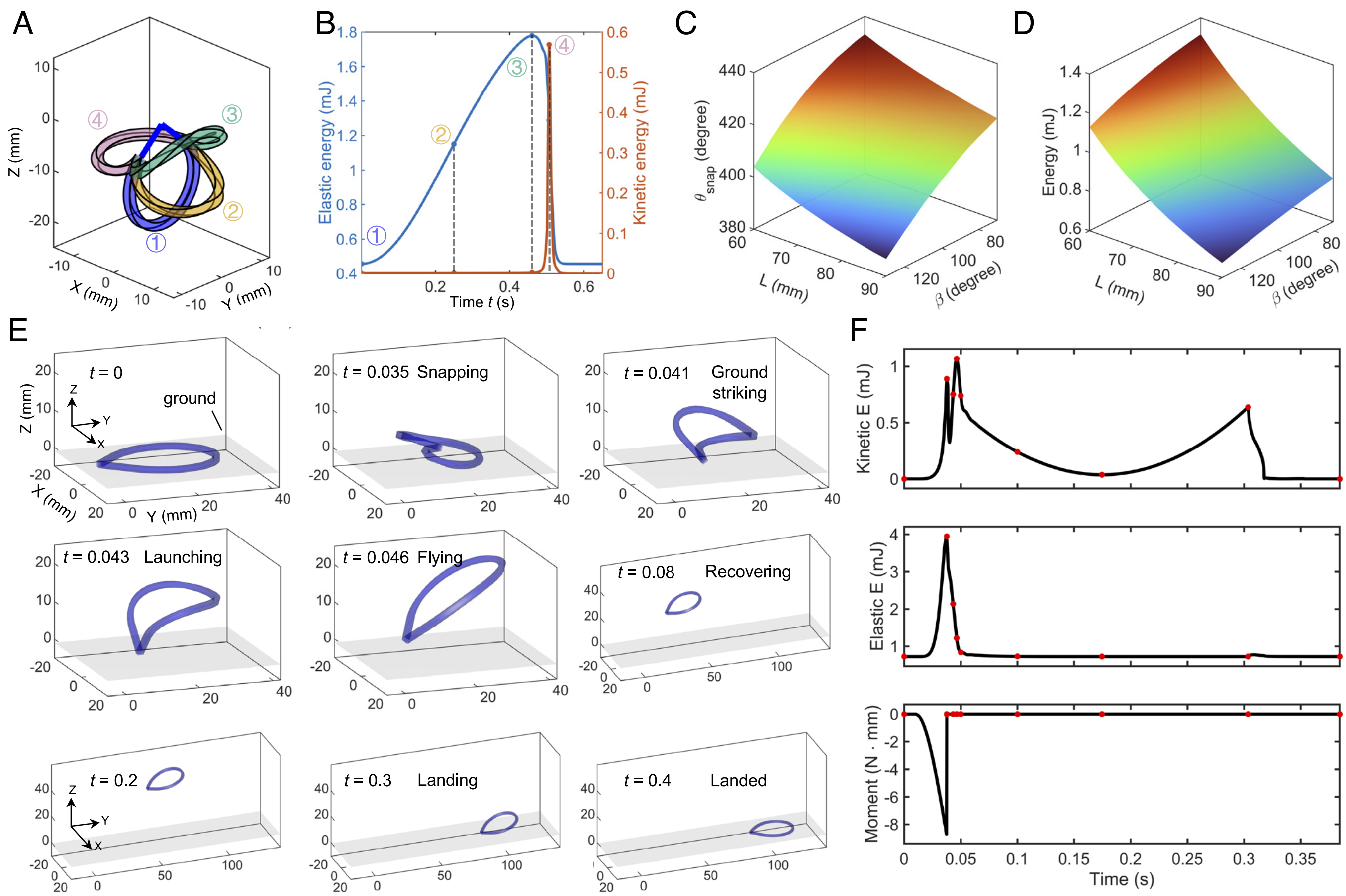

Fig. 3. Cosserat-rod modeling of snapping and jumping dynamics in the LCE ring jumper. (*A* and *B*) Dynamic Cosserat-rod of snap-through energy conversion, showing representative rod configurations (L = 60 mm and β = 95°) and the time evolution of elastic and kinetic energies. (*C* and *D*) Phase diagrams obtained from the static Cosserat-rod model, showing the snapping angle θ_{snap} and the elastic energy stored at the snapping configuration as functions β and L. (*E*) Full jumping simulation with ground contact. (*F*) Time evolution of the kinetic energy, elastic energy, and applied twist moment in the full jumping simulation, with red markers corresponding to the snapshots in (*E*).

the system follows a stable twisted equilibrium branch rather than exhibiting snapping, consistent with both experiments and previous reports (29–31). These results indicate that snapping in the LCE jumper does not arise from twisting alone, but from the coupled effects of twisting and the V-shaped tail geometry.

Finally, to simulate the complete leaping process including ground contact and friction, we employ PyElastica (33), an open-source Cosserat-rod simulation framework (*SI Appendix, Note S7*). Heating-induced actuation is simplified as a time-increasing twist moment applied along the ring. The ring interacts with the ground through normal contact and friction. The simulation reproduces the full sequence and energy evolution observed experimentally, including coupled twisting and bending, snapping, takeoff, flight, shape recovery through untwisting and unbending, and landing (Fig. 3 *E* and *F* and Movie S5, and more discussions in *SI Appendix, Note S6*).

Optimizing Controllable Leaping by Shifting the Center of Mass. The locomotion phase diagram in Fig. 2*A* reveals that stabilized leaping occurs only within a narrow design window, as backflips and alternating headings undermine directional control. This instability originates from misalignment between the center of mass (CoM) and thrust at liftoff, which generates torque and induces rotation at high launch angles. To broaden the design space and achieve controlled, longer leaps, we introduce a simple modification: attaching a copper-foil tube as a head weight (Fig. 4*A*). We define the weight ratio (wt%) as the added head mass relative to the net ring mass. As wt% increases from 0 to 36%, the CoM shifts progressively forward (Fig. 4*B* and *SI Appendix, Note S8*), suppressing flips, converting vertical jumps into forward leaps, and stabilizing trajectories for extended travel (Fig. 4*C*). This strategy echoes natural jumpers such as grasshoppers and fleas, which bias mass forward to stabilize and steer motion (34).

Theoretically, optimal leaping requires maximizing the horizontal component of translational speed while minimizing rotation. From projectile mechanics, leap distance follows $L = v^2 \sin(2\alpha)/g$, where v is launching speed, g is gravity, and the ideal launch angle is ~45°. Guided by this principle, we tune both β and wt% to maximize speed while achieving forward launch angles of 40° to 50° under optimal intermediate irradiance.

A representative case of a leaping ring with β = 100° illustrates the effect of mass redistribution (Fig. 4*C*). As wt% increases from 0 to 100%, as expected, its maximum jumping height decreases monotonically and dramatically when wt% is over 50% due to its increasing weight. However, horizontal leap distance first increases, peaking at ~50 mm for wt% ≈ 36%, before declining. This suggests that appropriate mass redistribution can enhance forward leap distance. Similar trends are observed across other β (*SI Appendix*, Fig. S10).

Maps of launch angle α and speed v as functions of β (60° to 120°) and wt% (0 to 33.5%) (Fig. 4 *D* and *E*) generalize these behaviors (*SI Appendix*, Fig. S11). Small β and low wt% produce unstable flips with high α and v (*SI Appendix*, Fig. S12). Increasing β or wt% lowers α by shifting the CoM forward, suppressing flips and enabling directional leaps (Fig. 4*F*). A clear phase boundary emerges: stable leaping requires $\alpha \le 59°$ and $v \le 0.46$ m/s. For example, sharp-angle vertical jumpers or unstable back-flippers (β = 60° to 80°) transition into forward leapers (α ~48° to 60°) with added head weight (Fig. 4 *F–H* and Movie S6). Although both β and wt% reduce launch speed via diminished elastic storage or added mass, β exerts the stronger effect. The optimal regime occurs at a launch angle of 40° to 50° and velocity exceeding 0.4 m/s, achieved at β = 80° and wt%=25% (Fig. 4*H*). This configuration yields the longest stabilized leaps of ~75 mm (~3.1 BLs) (Fig. 4 *G* and *H* and *SI Appendix*, Fig. S13), more than twice the distance of electrohydrostatically driven tethered soft jumpers (1.46 BLs) powered by high–energy-density dielectric actuators (3).

Leaping on sloped surfaces (Movie S7) presents additional challenges absent on flat ground. At launch, the incline reduces effective thrust and increases slip risk, while at landing, asymmetric impact and downslope gravity bias generate destabilizing torques that induce tumbling and hinder recovery. These effects compromise both efficiency and stability. CoM tuning, however, enables controlled leaping even on inclined terrain. On mild slopes (10°), increasing wt% from 12 to 36% suppresses backflips (Fig. 4*I*) and yields stable uphill leaps of ~1.8 BLs (Fig. 4*J*). Similarly, a moderate head weight effectively suppresses flips, enabling forward leaping on steep terrain despite minor slip (Fig. 4*K* and *SI Appendix*, Fig. S14).

Adaptive and Resilient Collisions With High Walls. To enable navigation in unstructured environments, it is essential for the leaping ring to possess collision resilience, i.e., the ability to sustain locomotion despite collisions. We investigate the ring's self-adaptative behavior after leaping against a high wall (Fig. 5*A*). To quantify ring–wall interactions, we introduce the attacking angle α_c, defined as the angle between the local tangent plane of the ring head and the vertical wall (Fig. 5 *A*, *Inset* and *SI Appendix*, Fig. S15).

Based on experimental observations, the postcollision behaviors can be broadly categorized into three representative modes: flipping, trapping, and rebounding, depending on the attacking angle (Fig. 5 *B–E* and Movie S8). When α_c is small ($\alpha_c < 18°$), the ring head hits the wall first, followed by its tail, leading to an upside-down flip (for example, $\alpha_c \sim 4°$ in Fig. 5*B*). Owing to the ring's mirror symmetry, the flipped ring reverses its heading upon landing and subsequently jumps away from the wall (Fig. 5*B*), as shown by the rapidly increasing head-wall traveling distance of over 4.5 BLs (~90 mm) after three leaps (Fig. 5*F*). The flipping mode occurs more frequently in rings with sharper binding angles ($\beta \le 70°$, Fig. 5*E*), where greater stored energy produces a higher head impact height.

For moderate angles ($18° < \alpha_c < 72°$), the ring strikes the wall obliquely, then falls and leans against the wall with its head rotated, becoming temporarily trapped between the wall and the ground (Fig. 5*C*). A subsequent launch, often triggered by striking its tail against the wall, enables the ring to escape. Flipping frequently occurs during this process, redirecting motion away from the wall. Compared with the flipping mode, the trapping mode results in a twice shorter head-wall distance (~2.2 BLs) after three leaps (Fig. 5*F*). This trapping behavior is more commonly observed in rings with moderate binding angles ($80° \le \beta \le 90°$, Fig. 5*E*).

When $\alpha_c > 72°$, the head impacts the wall nearly normally ($72° \le \alpha_c \le 90°$) or during the descending phase ($\alpha_c > 90°$, e.g., α_c ~110° in Fig. 5*D*). In this regime, the ring rebounds while retaining its heading toward the wall after landing, which is mostly observed in the rings with large binding angles ($\beta \ge 100°$) that possess lower jumping height (Fig. 5*E*). Subsequent impacts may still occur, with later interactions again falling into any of these three modes, as shown in one representative example of slightly increased head-wall distance (~0.6 BLs) after four leaps (Fig. 5*F*).

Moreover, compared with right-angle collisions, oblique side impacts from an angled moving pathway more effectively redirects the robot's moving direction angled away from the wall, without triggering flipping, trapping, and rebounding behaviors (Fig. 5*G*).

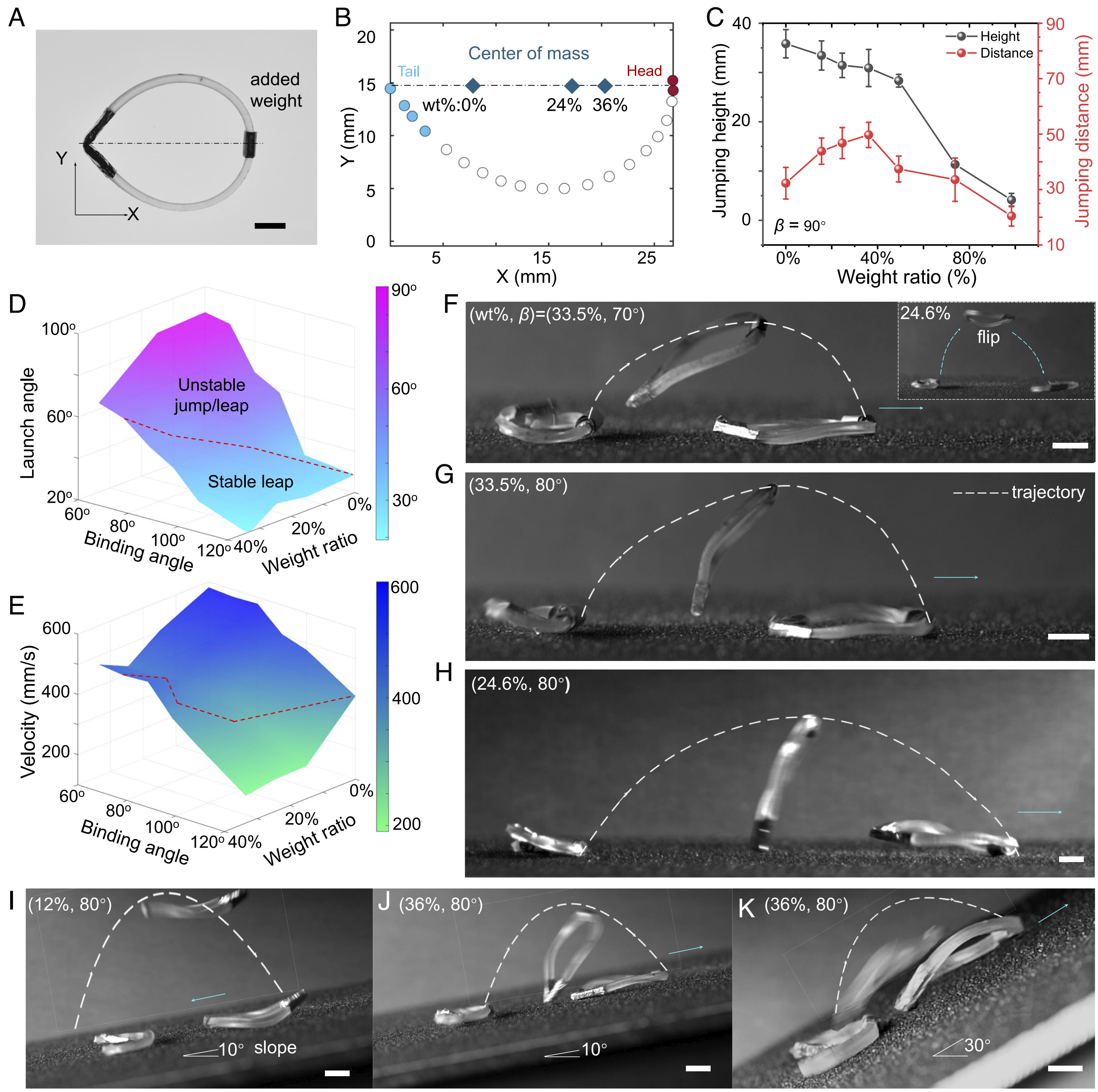

Fig. 4. Center-of-mass tuning enables robust and directional leaping. (*A*) Optical image of a ring with added head weight. (*B*) Forward shift of the center of mass with increasing head weight ratio (wt%, 0 to 36%). Blue, white, and red markers indicate the aluminum-covered tail, pure LCE body, and copper-covered head, respectively. (*C*) Jump height and leap distance versus wt% (β = 90°, w = 0.49 W cm^{-2}). (*D* and *E*) Phase maps of launch angle (*D*) and velocity (*E*) as functions of β and wt%. (*F*–*H*) Representative trajectories illustrating the evolution from backflipping (*F*, *Inset*) to stable forward leaping (*F* and *G*) and optimal, longest leap (~3.1 BLs) (*H*). (*I*–*K*) Transition from unstable backflip (*I*) to stable leaping (*J* and *K*) on inclined terrains (10° and 30° slopes) achieved through mass tuning. Dashed lines trace head trajectories. (Scale bar, 5 mm.)

Unstructured Environments With Natural Terrains. We next investigate continuous leaping in more realistic environments with multiple obstacles and natural terrains. In addition to the high-walls, obstacles that are not high enough to completely block the leaping trajectory are still common. To test this, we place two parallel hurdles (Fig. 6 *A* and *B* and Movie S9), each 5 mm high (~5 BHs) and spaced 27 mm apart (1.35 BLs). Two distinct outcomes emerge. In the first, the jumper performs clean clearance, leaping ~1.5 BLs to land between the hurdles before vaulting the second (Fig. 6*A*). In the second, collision-assisted clearance turns apparent failure into advantage: when the tail catches on the first hurdle, self-resetting twists the body downward, pressing the bent tail against the hurdle wall to generate extra thrust (Fig. 6*B*). This interaction produces a higher and longer leap (~2.2 BLs), enabling successful traversal of the second hurdle. Even against much taller barriers (~26 BHs), jumpers with sharp binding angles manage to vault despite impact (*SI Appendix*, Fig. S16 and Movie S10).

To further challenge the system, we simulate a "pillar forest" with randomly scattered tacks (5 BHs high; Fig. 6 *C* and *D* and Movie S11). The jumper occasionally becomes trapped or degrades

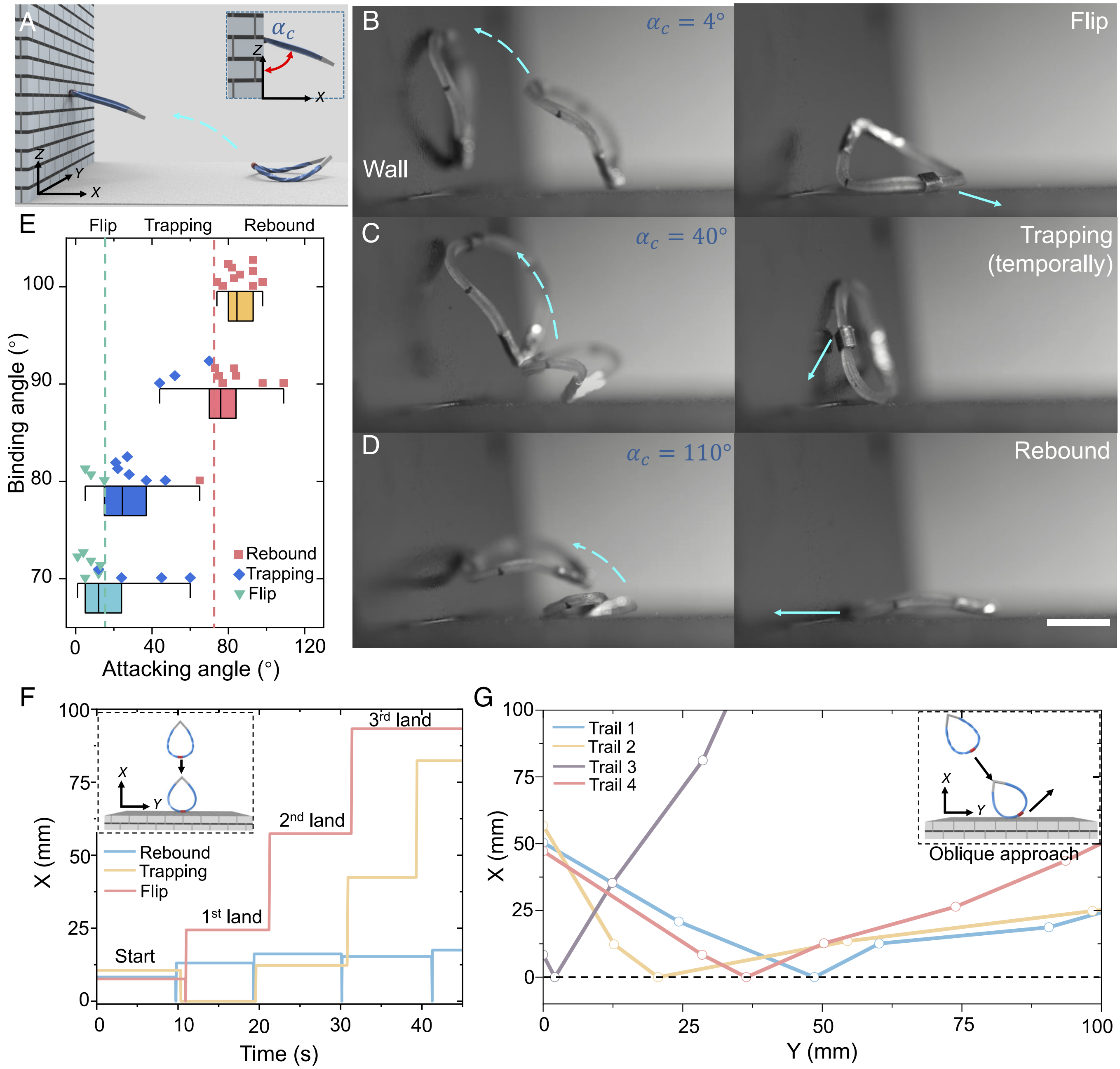

Fig. 5. Collision resilience of the leaping ring. (*A*) Schematic of the leaping ring hitting on a rigid high wall with an attacking angle α_c shown in the inset. (*B*–*D*) Three representative modes of postcollision behaviors for rings with small, moderate, and large α_c, respectively. (Scale bar, 10 mm.) (*E*) Statistical box plots on the correlation between the binding angle and the attacking angle on the postcollision behaviors. (*F*) The tracked position changes along the *X*-axis with time for the three representative collision modes over several consecutive leaps. (*G*) The tracked X–Y planar trajectories for four trials of oblique side impacts of a leaping ring with varying approaching angles. Inset shows schematic of the oblique collision.

into crawling, yet through six successive jumps and posture self-adjustments, it can eventually escape and reestablish forward leaping.

We then assess performance on natural terrains including gravels (*SI Appendix*, Fig. S17), grass, wet sand, and mulch (Movie S12). On grass (Fig. 6*E*), irregular and compliant surfaces induce erratic headings (Fig. 6*F*) but enable consistently high jumps (>4 BHs), enhancing speed despite reduced control. In contrast, motion on wet sand (Fig. 6*G*) requires more steps (8 jumps) and longer travel time, but trajectories are smoother and more predictable (Fig. 6*H*), as the yielding yet solid substrate stabilizes heading. Mulch exhibits intermediate behavior (Fig. 6*I*): irregularity occasionally traps the jumper or induces backward leaps, but overall predictability exceeds that of grass. Trajectory comparisons (Fig. 6 *F*, *H*, and *J*) reveal distinct terrain effects: over 100 mm of travel, sand and mulch support more consistent heading control than grass, with sand offering the most stable trajectories, mulch moderate unpredictability, and grass the fastest but least directed leaps.

Amphibious Multimodal Locomotion. Last, inspired by amphibious leaping organisms such as frogs, we explore the ring jumper's potential for multimodal locomotion across land–water interfaces by coating the ring with a hydrophobic layer (Fig. 7 *A*–*C* and *SI Appendix*, Fig. S18 and *Note S1* and *Methods*). Several challenges arise in enabling amphibious motions. First, compared with leaping on land, the tail–water interaction dissipates much of the impact energy, producing substantially lower thrust for

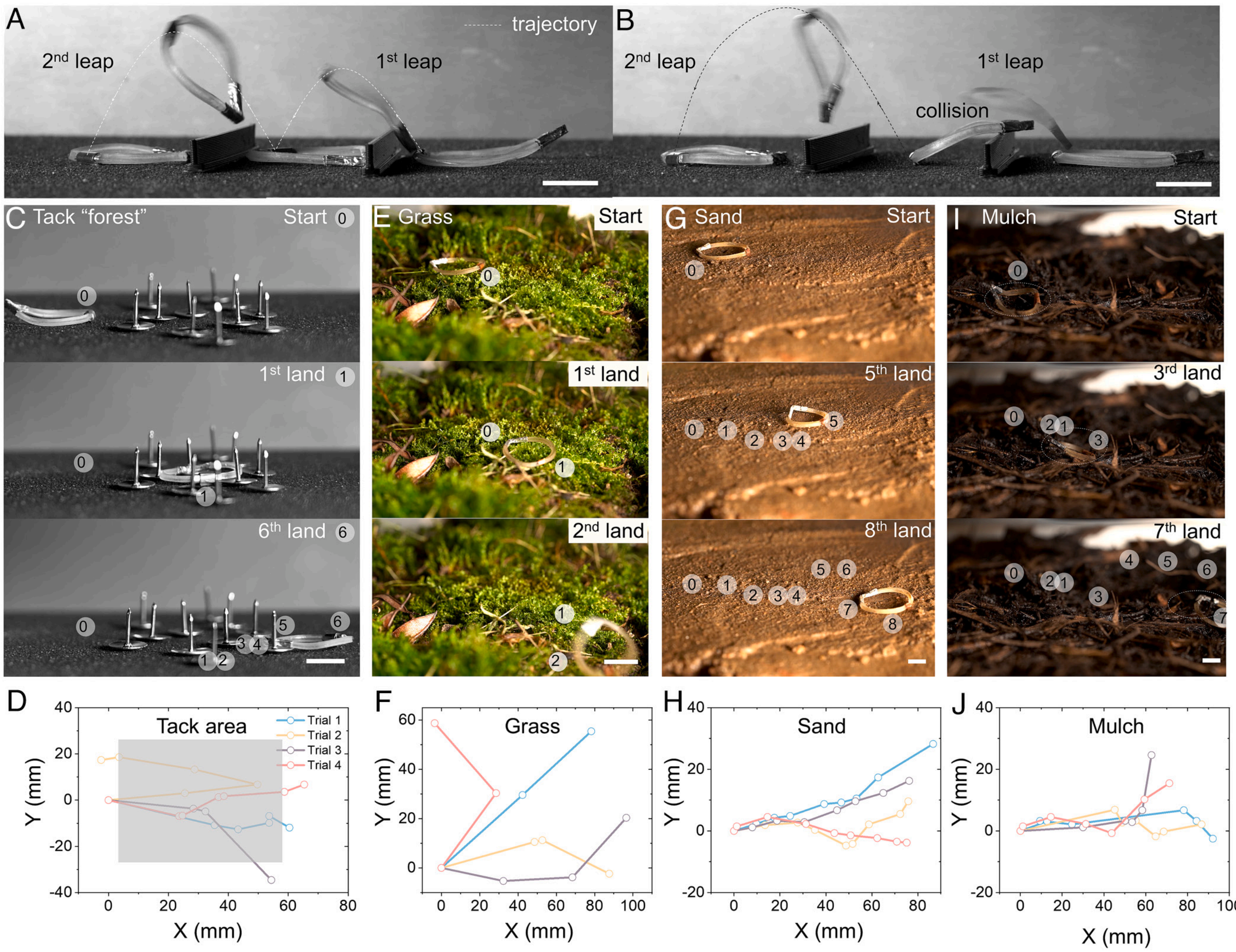

Fig. 6. Robust continuous leaping across obstacles and natural terrains. (*A* and *B*) Continuous jumping over two parallel hurdles (5 BHs high, 1.35 BLs apart) without (*A*) and with collision (*B*). (*C* and *D*) Navigation through randomly scattered tacks simulating a "pillar forest" (5 BHs high) with trajectories shown in *D*. (*E*–*J*) Leaping on natural terrains: grass (*E* and *F*), wet sand (*G* and *H*), and mulch (*I* and *J*).

propulsion. Second, given the ring's millimeter-scale size, water-to-land transition requires overcoming the surface-tension barrier without becoming trapped at the air–water interface (35). To enhance the thrust during surface swimming, we incorporate reduced graphene dioxide (rGO) into the LCE ring to increase light absorbance at the water surface, thereby generating stronger actuation forces. We also introduce an extended square-shaped tail to further improve propulsion (Fig. 7 *A* and *B* and *SI Appendix*, Figs. S19 and S20).

The multimodal locomotion is demonstrated through series of behaviors, including land-to-water jumping (Fig. 7*D* and *SI Appendix*, Fig. S21), surface swimming, and water-to-land transitioning (Movie S13). After leaping from land into water, the hydrophobic ring floats and drifts on the water surface. Under IR illumination, similar to its behavior on land, twisting of the floating body leads to tail rotation and snapping, which pushes water backward and propels the ring swimmer forward through tail paddling (Fig. 7*E* and *SI Appendix*, Fig. S22). Despite the lower surface temperature and reduced actuation strain of the LCE body in water compared with on land (*SI Appendix*, Fig. S20), water dissipates heat much more quickly than air, resulting in a significantly shorter actuation cycle during swimming (~1 s) than during leaping on land (~20 s). After reaching an inclined shoreline, it transitions from swimming to jumping by striking the slope underwater. The snapping of the extended tail then provides a stronger driving force, enabling the ring to break through the air–water surface-tension barrier and land on the substrate (Fig. 7*F*). In more cluttered natural settings, such as water surfaces covered with floating leaves (e.g., lotus or tree leaves), the ring jumper can leap, swim, and crawl across the leaves, demonstrating its ability to navigate complex aquatic environments in natural terrains (*SI Appendix*, Fig. S23).

Discussion

We demonstrate a geometry-enabled self-resetting soft ring that achieves sustained, directional leaping under uniform infrared illumination, addressing the long-standing challenge of continuous operation in soft jumping systems. The V-shaped tailed-ring geometry enables compact and efficient energy storage through twisting, while spontaneous untwisting during flight restores the original shape for autonomous relaunch regardless of landing orientation. During interactions with obstacles, the ring's mirror symmetry provides high collision resilience and enables adaptive reorientation of locomotion. By tuning the center of mass, the system can further stabilize and self-regulate its motion across slopes, obstacles, and diverse natural terrains. The soft ring exhibits robust multimodal locomotion across environments with varying

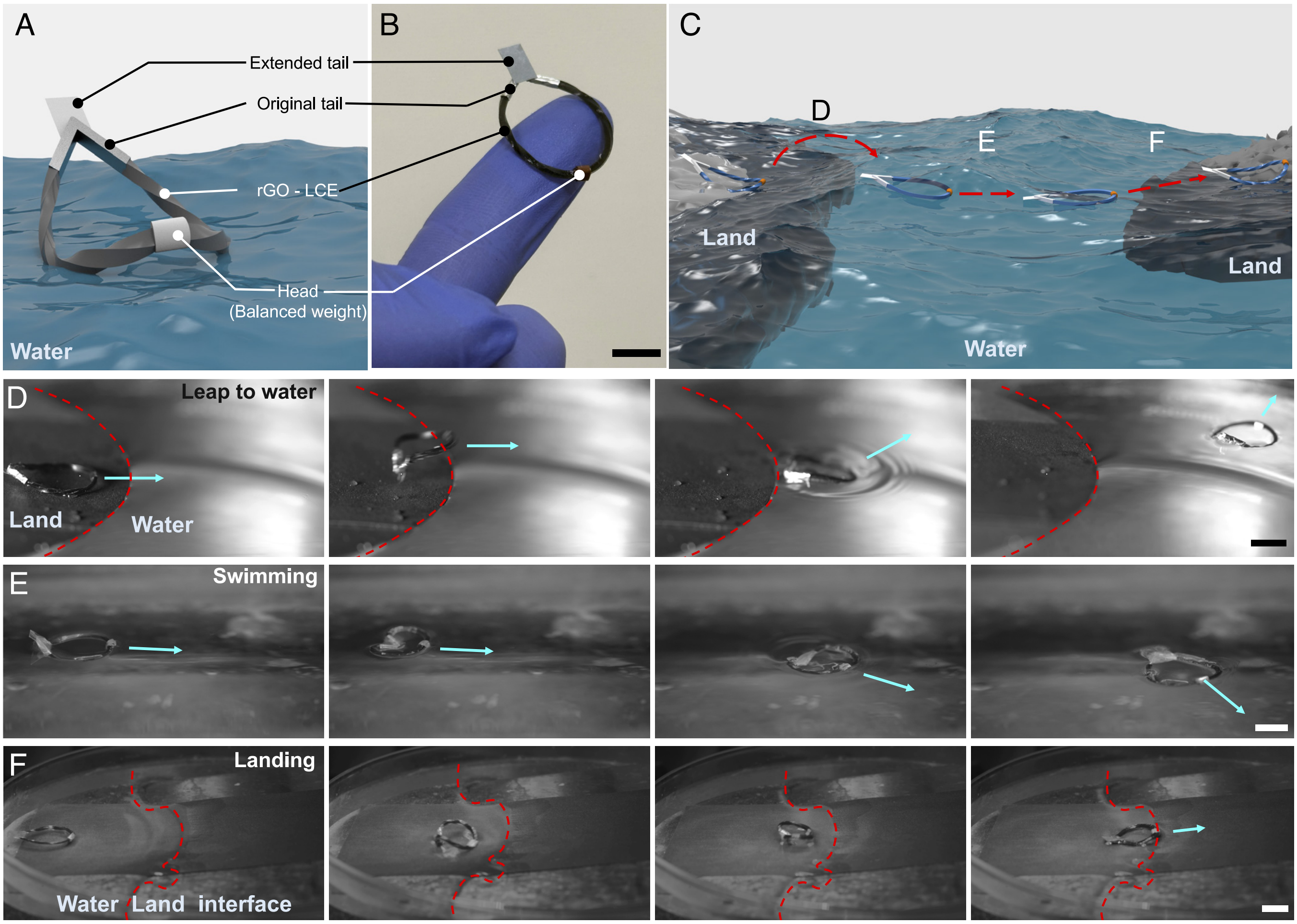

Fig. 7. Amphibious multimodal jumping and swimming. (*A* and *B*) Schematic and image of the amphibious leaping ring with an extended tail, hydrophobic coating, and mixed reduced graphene oxide (rGO). (*C*) Schematic of multimodal land–water, water surface, and water–land transitions. (*D*) Leaping from land to water surface. The red dashed line marks the land–water interface. (*E*) Swimming on water surface via tail paddling. (*F*) Transitioning from water to land via leaping to break the surface tension barrier of the water–land interface (red dashed line). (Scale bar, 10 mm.)

compliance, surface roughness, and land–water interfaces, highlighting its potential for autonomous navigation in unstructured environments.

Compared with previous studies on snapping rings and soft jumping systems, the present work is distinguished both fundamentally and functionally (*SI Appendix*, *Note S9*). From a mechanics perspective, the snapping instability observed in our LCE ring jumper differs fundamentally from classical Michell-type twist instabilities (36) and previously reported snapping-ring systems (37). In classical elastic rings with circular cross-sections, a planar equilibrium branch persists under small imposed twist and loses stability only beyond a critical twist threshold, leading to bifurcation into an out-of-plane configuration (36). By contrast, our ring combines a noncircular square cross-section with anisotropic bending stiffness and a rigid V-shaped tail, causing twist to couple immediately with bending and out-of-plane deformation. Consequently, the structure evolves through fully three-dimensional equilibrium states from the onset of actuation. Unlike previous ring-origami and twisted-ring systems, which rely on programmed geometry, residual strain, or external loading to trigger snap-folding (37), the present LCE ring accumulates elastic energy directly through actuation, without external preloading. The snapping transition instead emerges from the coupled effects of anisotropic cross-sectional stiffness, continuous twist actuation, rigid-body geometric constraints, and the binding angle introduced by the tailed-ring architecture. Accordingly, the instability is identified not through the loss of stability of a planar equilibrium branch, but through the loss of regularity of the full three-dimensional Cosserat-rod equilibrium Jacobian near the critical snapping state.

Moreover, the resulting continuous jumping behavior differs fundamentally from the self-sustained but nonjumping motions reported in previous soft ring systems (29–31, 38). For example, nylon fiber rings (31) and twisted LCE rings (29) exhibit continuous self-flipping or coupled flip–spin–orbit motion on heated surfaces without snapping-induced jumping. Similarly, both 2D (38) and 3D wavy LCE rings (30) can display repetitive self-flipping through snapping, yet fail to achieve jumping because of insufficient elastic energy storage. These previously reported systems generally retain highly symmetric circular ring geometries. In contrast, our design deliberately breaks circular symmetry by integrating a soft ring with a rigid V-shaped tail, thereby dramatically enhancing elastic energy storage and directional asymmetry to enable sustained snapping and continuous directional leaping under constant external fields.

Last, the self-resetting capability for autonomous shape recovery, repeated landing, and relaunch, without spatiotemporal control of actuation inputs, is largely absent in existing soft jumpers (3, 7, 11, 18, 20, 22, 24–26) (Fig. 1*E* and *SI Appendix*, Table S1). Rather than relying on electronic feedback, onboard control, or externally timed actuation, the present design exploits the asymmetric V-shaped ring geometry to achieve self-regulated energy storage, release, and resetting. Many existing designs rely on bistable snap-through mechanisms that require manual resetting before subsequent jumps (3, 7, 11, 18, 20, 22, 24, 25). Others employ structure fracturing to trigger launch, inherently limiting operation to a single use due to material damage (11). Repetitive soft jumpers driven by externally timed actuation can achieve multiple cycles, but typically depend on controlled impulse inputs functioning as artificial "latches" to reset the system (3). Although recent strategies based on evaporation-driven actuation (27) or light-shadowing effects (28) demonstrate autonomous resetting, their jumping performance and environmental adaptability remain limited. Specifically, evaporative elastomer disks suffer from long cycle times and primarily produce upright jumping (27), while shadowing-induced self-shuttering systems are highly sensitive to illumination direction (28), restricting their ability to traverse sloped or cluttered terrains. In contrast, our self-resetting ring sustains multimodal locomotion across complex environments and further combines jumping and swimming to navigate challenging land–water interfaces.

Despite these advances, several limitations remain. Achieving precise directional control during continuous leaping in cluttered environments remains challenging due to the stochastic contact conditions. In addition, the theoretical model provides a simplified mechanical description of the LCE ring jumper and does not fully capture the coupled thermal and nonlinear material behavior involved in photothermal actuation. Instead, the model primarily reveals the geometric and mechanical origin of snapping instability and jumping. Future work could incorporate fully coupled thermo-mechanical modeling and environmental interactions to improve predictive accuracy. Moreover, the locomotion range is currently constrained by the spatial coverage of the externally supplied infrared illumination. Future implementations may further integrate wireless energy transfer or harvest ambient energy, such as natural sunlight, to achieve fully untethered autonomous operation.

Methods

The LCE rings were fabricated by bending a LCE rod synthesized through two-stage curing and binding its ends with a thin aluminum tube, while the amphibious rings were fabricated by adding rGO powder (~2%) during the first-stage curing of LCE rods, and dip-coating a hydrophobic Ecoflex coating with an attached PET tail after second-stage curing. Detailed fabrication methods are described in *SI Appendix*, *Note S1*. The LCE jumpers were actuated using one or more infrared emitters (250W, REPTI ZOO) with their motion captured by high-speed cameras and details described in *SI Appendix*, *Note S2*.

Data, Materials, and Software Availability. Study data are included in the article and/or supporting information.

ACKNOWLEDGMENTS. J.Y. acknowledges the funding support from the NSF under award number CMMI-2329674, 2445551, and 2527304.

Author affiliations: [a]Department of Mechanical and Aerospace Engineering, North Carolina State University, Raleigh, NC 27695

1. Y. Chi *et al.*, Bistable and multistable actuators for soft robots: Structures, materials, and functionalities. *Adv. Mater.* **34**, 2110384 (2022).
2. B. Gorissen, D. Melancon, N. Vasios, M. Torbati, K. Bertoldi, Inflatable soft jumper inspired by shell snapping. *Sci. Robot.* **5**, eabb1967 (2020).
3. R. Chen *et al.*, Legless soft robots capable of rapid, continuous, and steered jumping. *Nat. Commun.* **12**, 7028 (2021).
4. D. Luo *et al.*, Autonomous self-burying seed carriers for aerial seeding. *Nature* **614**, 463–470 (2023).
5. A. Yamada, H. Mameda, H. Mochiyama, H. Fujimoto, "A compact jumping robot utilizing snap-through buckling with bend and twist" in *2010 IEEE/RSJ International Conference on Intelligent Robots and Systems* (2010), pp 389–394.
6. S. Spiegel, J. Sun, J. Zhao, A shape-changing wheeling and jumping robot using tensegrity wheels and bistable mechanism. *IEEE/ASME Trans. Mechatron.* **28**, 2073–2082 (2023).
7. D. Tang *et al.*, Bistable soft jumper capable of fast response and high takeoff velocity. *Sci. Robot.* **9**, eadm8484 (2024).
8. Q. Guo *et al.*, Bistable insect-scale jumpers with tunable energy barriers for multimodal locomotion. *Adv. Sci.* **11**, 2404404 (2024).
9. S. Kumar *et al.*, Reversible kink instability drives ultrafast jumping in nematodes and soft robots. *Sci. Robot.* **10**, eadq3121 (2025).
10. C. Hong *et al.*, Magnetically actuated gearbox for the wireless control of millimeter-scale robots. *Sci. Robot.* **7**, eabo4401 (2022).
11. X. Wang *et al.*, Fracture-driven power amplification in a hydrogel launcher. *Nat. Mater.* **23**, 1428–1435 (2024).
12. M. T. Tolley *et al.*, "An untethered jumping soft robot" in *2014 IEEE/RSJ International Conference on Intelligent Robots and Systems* (2014), pp 561–566.
13. N. W. Bartlett *et al.*, A 3D-printed, functionally graded soft robot powered by combustion. *Science* **349**, 161–165 (2015).
14. J. Brackenbury, H. Hunt, Jumping in springtails: Mechanism and dynamics. *J. Zool.* **229**, 217–236 (1993).
15. T. Lindtner, A. Y. Uzan, M. Eder, B. Bar-On, R. Elbaum, Repetitive hygroscopic snapping movements in awns of wild oats. *Acta Biomater.* **135**, 483–492 (2021).
16. P. Marmottant, A. Ponomarenko, D. Bienaimé, The walk and jump of Equisetum spores. *Proc. R. Soc. B: Biol. Sci.* **280**, 20131465 (2013).
17. H. Seung Choi, D. Seok Kim, Self-repeatable snapping liquid-crystal-elastomer actuator. *Chem. Eng. J.* **500**, 156744 (2024).
18. B. Lei, Z.-Y. Wen, H.-K. Wang, J. Gao, L.-J. Chen, Bioinspired jumping soft actuators of the liquid crystal elastomer enabled by photo-mechanical coupling. *ACS Appl. Mater. Interfaces* **16**, 1596–1604 (2024).
19. T. S. Hebner, K. Korner, C. N. Bowman, K. Bhattacharya, T. J. White, Leaping liquid crystal elastomers. *Sci Adv.* **9**, eade1320 (2023).
20. J. Hu *et al.*, Springtail-inspired light-driven soft jumping robots based on liquid crystal elastomers with monolithic three-leaf panel fold structure. *Angewandte Chemie International Edition* **62**, e202218227 (2023).
21. Z. Deng, K. Li, A. Priimagi, H. Zeng, Light-steerable locomotion using zero-elastic-energy modes. *Nat. Mater.* **23**, 1728–1735 (2024).
22. M. Duduta *et al.*, Electrically-latched compliant jumping mechanism based on a dielectric elastomer actuator. *Smart Mater. Struct.* **28**, 09LT01 (2019).
23. Y. Wang *et al.*, Amphibious miniature soft jumping robot with on-demand in-flight maneuver. *Adv. Sci.* **10**, 2207493 (2023).
24. J. Li *et al.*, Recent development of jumping motions based on soft actuators. *Adv. Funct. Mater.* **33**, 2300156 (2023).
25. Y.-H. Hsiao *et al.*, Hybrid locomotion at the insect scale: Combined flying and jumping for enhanced efficiency and versatility. *Sci. Adv.* **11**, eadu4474 (2025).
26. E. W. Hawkes *et al.*, Engineered jumpers overcome biological limits via work multiplication. *Nature* **604**, 657–661 (2022).
27. Y. Kim, J. van den Berg, A. J. Crosby, Autonomous snapping and jumping polymer gels. *Nat. Mater.* **20**, 1695–1701 (2021).
28. W. Yan *et al.*, Self-sustained, continuous jumping of a light-driven electronics-free insect-scale soft robot. *Adv. Mater.* **37**, e19669 (2025).
29. F. Qi *et al.*, Defected twisted ring topology for autonomous periodic flip–spin–orbit soft robot. *Proc. Natl. Acad. Sci. U.S.A.* **121**, e2312680121 (2024).
30. Y. Zhao *et al.*, Self-sustained snapping drives autonomous dancing and motion in free-standing wavy rings. *Adv. Mater.* **35**, 2207372 (2023).
31. A. Baumann *et al.*, Motorizing fibres with geometric zero-energy modes. *Nat. Mater.* **17**, 523–527 (2018).
32. J. Till, V. Aloi, C. Rucker, Real-time dynamics of soft and continuum robots based on Cosserat rod models. *Int. J. Robot. Res.* **38**, 723–746 (2019).
33. M. Gazzola, L. H. Dudte, A. G. McCormick, L. Mahadevan, Forward and inverse problems in the mechanics of soft filaments. *R. Soc. Open Sci.* **5**, 171628 (2018).
34. M. F. Bobbert, G. J. van Ingen Schenau, Coordination in vertical jumping. *J. Biomech.* **21**, 249–262 (1988).
35. Y. Chen, N. Doshi, B. Goldberg, H. Wang, R. J. Wood, Controllable water surface to underwater transition through electrowetting in a hybrid terrestrial-aquatic microrobot. *Nat. Commun.* **9**, 2495 (2018).
36. A. Goriely, Twisted elastic rings and the rediscoveries of Michell's instability. *J. Elast.* **84**, 281–299 (2006).
37. L. Lu, S. Leanza, J. Dai, J. W. Hutchinson, R. R. Zhao, Multistability of segmented rings by programming natural curvature. *Proc. Natl. Acad. Sci. U.S.A.* **121**, e2405744121 (2024).
38. D. S. Kim, Y.-J. Lee, Y. B. Kim, Y. Wang, S. Yang, Autonomous, untethered gait-like synchronization of lobed loops made from liquid crystal elastomer fibers via spontaneous snap-through. *Sci. Adv.* **9**, eadh5107 (2023).